# Designer Ionic Liquids for Reversible Electrochemical Deposition/Dissolution of Magnesium

Tylan Watkins, Ashok Kumar, and Daniel A. Buttry*

School of Molecular Sciences, Arizona State University, Tempe, Arizona 85287-1604, United States

S *Supporting Information*

ABSTRACT: Chelating ionic liquids (ILs), in which polyether chains are pendent from the organic pyrrolidinium cation of the ILs (PEGylated ILs), were prepared that facilitate reversible electrochemical deposition/dissolution of Mg from a $Mg(BH_4)_2$ source. Mg electrodeposition processes in two specific PEGylated-ILs were compared against that in the widely studied N-butyl-N-methylpyrrolidinium bis(trifluoromethylsulfonyl)imide ionic liquid (BMPyrTFSI). The two chelating IL systems (one with a pendent polyether chain with three ether oxygens, MPEG$_3$PyrTFSI, and the other with a seven-ether chain, MPEG$_7$PyrTFSI) showed substantial improvement over BMPyrTFSI for Mg electrodeposition/dissolution. The best overall electrochemical performance was in MPEG$_7$PyrTFSI. X-ray diffraction (XRD), scanning electron microscopy (SEM), and energy dispersive X-ray spectroscopy (EDS) were used to characterize galvanostatically deposited Mg, revealing production of pure, dendrite-free Mg deposits. Reversible Mg electrodeposition was achieved with high Coulombic efficiency (CE) of 90% and high current density (ca. 2 mA/cm^2 for the stripping peak). Raman spectroscopy was used to characterize Mg^{2+} speciation in the PEGylated ILs and BMPyrTFSI containing $Mg(BH_4)_2$ by study of Raman modes of the coordinated and free states of borohydride, TFSI$^-$, and polyether COC groups. Quantitative analysis revealed that the polyether chains can displace both TFSI$^-$ and BH$_4^-$ from the coordination sphere of Mg^{2+}. Comparison of the different IL electrolytes suggested that these displacement reactions may play a role in enabling Mg deposition/dissolution with high CE and current density in these PEGylated IL media. These results represent the first demonstration of reversible electrochemical deposition/dissolution of Mg in an ionic liquid specifically designed with this task in mind.
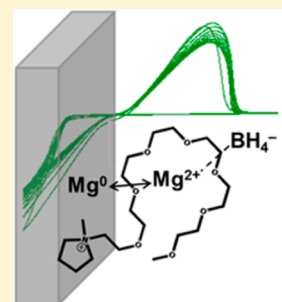
■ INTRODUCTION

The realization of reliable battery chemistries beyond the present Li-ion systems is an important goal in the field of energy conversion and storage. The theoretical metrics of a rechargeable battery using a metallic magnesium anode (3832 mAh/cm^3 volumetric and 2205 mAh/g gravimetric capacities) have motivated significant efforts to develop electrolytes and cathode materials for secondary Mg batteries.[1−4] The fundamental requirement for an electrolyte to be compatible with the (electro)chemistries of both the cathode and anode is not trivially met in Mg-based systems. For instance, simple Mg electrolytes analogous to those of typical Li battery chemistries have yet to show reversible electrodeposition of Mg metal. To date, most reported Mg electrolytes have been derived from organometallic sources, predominantly Grignard reagents or analogues, often in concert with AlR$_x$Cl$_{3-x}$ (R = alkane or aryl group) to provide increased oxidative stability. In some recent systems, the $[(\mu\text{-Cl})_3Mg_2(THF)_6]^+$ dimer and/or the [MgCl-(THF)$_5$]$^+$ monomer have been implicated in producing reversible electrochemical deposition and dissolution.[5] These various systems have shown reversible electrodeposition of dendrite-free Mg with high Coulombic efficiencies and reasonable oxidative stabilities.[4] However, halide electrolytes can be corrosive toward typical current collecting metals, limiting their commercial applicability.[6−9] Many Mg electrolytes also have unattractive safety characteristics due to use of

Grignards and/or tetrahydrofuran (THF) in the electrolyte.[2] Oligoether glymes have also been proposed as solvent systems for Mg electrolytes due in part to their lower volatility and higher thermal stabilities compared to THF.[10−13] We describe here an effort to develop Mg battery electrolytes that mitigate the above drawbacks.

In 2012 Mohtadi et al. demonstrated $Mg(BH_4)_2$ in tetrahydrofuran (THF) and dimethoxyethane (DME, also known as monoglyme or glyme) as the first fully inorganic and non-halide-containing Mg electrolytes to show reversible Mg deposition and stripping.[14] The $Mg(BH_4)_2$ solutions were also compatible with Mg^{2+} insertion into a Mo_6S_8 Chevrel cathode—one of the only cathodes reported to have good reversibility for Mg^{2+} insertion.[15] Other reports on $Mg(BH_4)_2$ electrolytes have followed with particularly interesting insights into the solvated structure dependence on the electrochemistry and the synergistic role played by LiBH$_4$ when added to enhance the current response.[11−13,16−18] Specifically, it has been argued that longer chain oligoether glyme solvents enhance the electrochemical Mg deposition/dissolution process due to increased electron donicity and chelating abilities of the chains.[17] This suggests that solvent systems containing polyethers may be attractive for reversible Mg deposition/

dissolution. It has also been shown that LiBH$_4$ aids the Mg deposition/dissolution process by co-depositing a small quantity of Li, providing another strategy for improving reversible deposition and dissolution.[17,18]

While the ether and polyether electrolytes appear promising, ideal electrolytes would be completely nonvolatile, nonflammable, and thermally stable up to high operating temperatures. This has led many groups to explore the use of ionic liquids (ILs) as electrolytes for a variety of battery systems. Many IL-based electrolytes have advantageous properties for Li-ion and post-Li-ion battery chemistries.[19] For instance, many tend to be nonvolatile and nonflammable, with high thermal stability, good conductivity, and a wide electrochemical window. However, despite these strengths, IL-based electrolytes have so far been hindered by high costs, relatively low rate capabilities, or generally poor performance, and have yet to find true commercial interest.

Ionic liquids have recently been explored as electrolytes for Mg battery systems, but so far with only limited success.[20−29] We report here for the first time reversible Mg electro-deposition/dissolution from a purely ionic liquid medium—designed to specifically enhance the Mg deposition/dissolution process. These results were achieved by synthesizing task specific ILs to meet the specific coordination conditions required for Mg deposition/dissolution from a Mg(BH$_4$)$_2$ source. A previous Raman spectroscopic study of the speciation state of Mg^{2+} in IL and glyme-containing IL electrolytes informed the structures of the ILs reported here, one of which has not yet been reported.[26] IL cations were synthesized in which methoxy terminated polyethylene glycol (PEG) chains were made pendent on methylpyrrolidinium cations (labeled MPEG$_m$Pyr$^+$ where M = methyl, m = number of ether oxygens in the PEG chain, and Pyr = pyrrolidinium) in ionic liquids containing bis(trifluoromethylsulfonyl)imide (TFSI$^-$) anions as the counterion. We show that these "PEGylated" ILs (Scheme 1) facilitate Mg deposition/dissolution. These task specific ILs

Scheme 1. General Molecular Structure for PEGylated Ionic Liquids Used in This Study
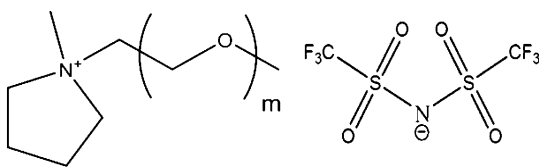
are shown to chelate Mg^{2+} and are therefore termed "chelating ILs". This is consistent with previous terminology used by Kar et al., in which chelating ILs were used in electrolytes containing Zn^{2+}.[30]

The results presented here are informed by recent work from Giffin et al. on crystal structures and liquid state properties of materials containing Mg(TFSI)$_2$ and N-methoxyethyl-N-methylpyrrolidinium TFSI,[31] and also by a recent Raman study reported by us on speciation of Mg^{2+} in ILs containing TFSI$^-$ and various ether and polyether solvents.[26] Here we compare the electrochemical characteristics of task specific, chelating ILs, containing Mg(BH$_4$)$_2$ to an analogous, non-chelating, IL electrolyte. We show that proper control of Mg^{2+} speciation can provide reversible electrochemical deposition and dissolution with Coulombic efficiencies over 90% and dendrite-free morphologies. These results represent the first demonstration of reversible electrochemical deposition/dis-

solution of Mg in an ionic liquid designed specifically for improved Mg electrochemical behavior.

■ EXPERIMENTAL SECTION

Chemicals. Lithium bis(trifluorosulfonyl)imide (99.5%, TCI America), sodium iodide (99.5%, EMD Millipore), 4-toluensulfonyl chloride (≥98%, Oakwood Chemical), iodobutane (synthetic grade, EMD Millipore), isopropyl alcohol (IPA) (99.7%, Alfa Aesar), triethylene glycol monomethyl ether (≥97%, Sigma Aldrich), sodium thiosulfate (99%, Sigma Aldrich), activated carbon (decolorizing, Sigma Aldrich), and methoxypolyethylene glycol, MW 350 (reagent grade, Sigma Aldrich) were used as received. Prior to use in their respective reactions ethyl acetate (99.5%, BDH), N-methyl pyrrolidine (97%, Sigma Aldrich), pyridine (≥99%, Sigma Aldrich), and dichloromethane (reagent grade BDH) were distilled over CaH$_2$. Acetone (Sigma Aldrich) was dried via 3 Å molecular sieves prior to a single distillation before use. Toluene (Lab Chem Inc.) was distilled over sodium and benzophenone prior to use.

Synthesis of Ionic Liquids. *1-(2-(2-(2-Methoxyethoxy)ethoxy)-ethyl)-1-methylpyrrolidinium Bis(trifluoromethylsulfonyl)imide (MPEG$_3$PyrTFSI).* The general procedure was a scaled up synthesis taken from Dobbelin et al.[32] However, we found work up of the PEG$_3$I was best performed using a 5% aqueous solution of sodium thiosulfate, as described below for synthesis of MPEG$_7$PyrTFSI. We also added an additional step of dissolving the final product in a small volume of IPA and stirred over activated charcoal at 40 °C overnight for purification. The final product was a lightly yellow-tinted liquid. *MPEG$_3$PyrTFSI:* ^{1}H NMR (400 MHz, (CD$_3$)$_2$CO) δ 4.06−4.01 (m, 2H, NCH$_2$CH_2O), 3.78−3.74 (m, 6H, NCH_2), 3.69−3.65 (m, 2H, OCH_2CH$_2$O), 3.63−3.6 (m, 4H, OCH_2CH_2O), 3.58−3.56 (m, 2H, OCH_2CH$_2$O), 3.48−3.45 (m, 2H, OCH_2CH$_2$O), 3.29 (s, 3H, OCH_3), 3.28 (s, 3H, NCH_3), 2.33−2.27 (m, 4H, CH_2CH_2). The ^{1}H NMR spectrum is shown toward the end of the Supporting Information.

Methoxypolyethylene Glycol (MW 350) Bis-(trifluoromethylsulfonyl)imide(MPEG$_7$PyrTFSI). The general procedure was taken from Ganapatibhotla et al. and adapted for pyrrolidinium-based cations as opposed to imidazolium cations.[33] 4-toluenesulfonyl chloride in dichloromethane was added dropwise to a solution of methoxypolyethylene glycol MW 350 and pyridine in dichloromethane at 0 °C to −10 °C and subsequently allowed to gradually warm back to room temperature as the reaction progressed overnight. After workup of the PEGylated tosyl (PEG$_7$Ts) product, described by Ganapatibhotla et al., NaI powder was slowly added to PEG$_7$TS/acetone at room temperature and allowed to react overnight. The PEGylated iodide (PEG$_7$I) product was worked up, again as described by Ganapatibhotla et al., by three 50 mL extractions using a 5% aqueous solution of sodium thiosulfate. The PEG$_7$I/toluene was then added to methylpyrrolidine and allowed to react at room temperature for 2 days. The resulting MPEG$_7$PyrI IL was separated from the toluene organic phase and extracted three times with 50 mL of diethyl ether. It was then dissolved in water and stirred with decolorizing activated carbon overnight. Finally, after filtering the carbon, the MPEG$_7$PyrI was combined with LiTFSI in water to give MPEG$_7$PyrTFSI. The MPEG$_7$PyrTFSI was rinsed three times with 18 MΩ water, then diluted with IPA and stirred in activated charcoal at 40 °C overnight for final purification. The IL was then dried at 80 °C, under 0.4 mTorr vacuum, for ≥17 h prior to use. The final product was a clear liquid. *MPEG$_7$PyrTFSI:* ^{1}H NMR (400 MHz, (CD$_3$)$_2$CO) δ 4.10−4.05 (m, 2H, NCH$_2$CH_2O), 3.79−3.77 (m, 6H, NCH_2), 3.70−3.68 (m, 2H, OCH_2CH$_2$O), 3.63−3.6 (m, 4H, OCH_2CH_2O), 3.58−3.56 (m, 2H, OCH_2CH$_2$O), 3.48−3.45 (m, 2H, OCH_2CH$_2$O), 3.29 (s, 3H, OCH_3), 3.28 (s, 3H, NCH_3), 2.33−2.27 (m, 4H, CH_2CH_2). The ^{1}H NMR spectrum is shown at the end of the Supporting Information.

Raman Spectroscopy. Raman samples were prepared and spectra acquired as described in a recent report on [Mg-(TFSI)$_2$]$_x$[BMPyrTFSI]$_{1−x}$ ILs.[26] Stoichiometric amounts of Mg-(BH$_4$)$_2$ were combined with each of the ILs, and mixing was conducted at 70−100 °C until homogeneous solutions were produced. All Raman spectra were acquired at room temperature. Raman data

were collected using a custom built Raman spectrometer in a 180° geometry. The samples were excited using a 100 mW Compass 532 nm laser. The laser power was controlled using neutral density filters. The laser was focused onto the sample using a 50× super-long working distance Mitutoyo objective lens with a numerical aperture of 0.42. The signal was discriminated from the laser excitation using a Kaiser Laser band-pass filter followed by a Semrock edge filter. The data were collected using an Acton 300i spectrograph and a back-thinned Princeton Instruments liquid-nitrogen cooled CCD detector. For the regions of interest, measurements were made with an 1800 nm grating from 50 to 1200 cm^{-1} (1 cm^{-1} resolution). Spectra were acquired for 10 s five times for adequate signal-to-noise levels.

A custom-made Matlab GUI was used to fit pseudo-Voigt functions in the 715−775 cm^{-1} region (described in the Results and Discussion), in which the Lorentzian/Gaussian characters and fwhm could be varied manually, to the raw data (fits were made with the same general parameters as described in ref 26). All raw spectra were corrected with use of a cyclohexane standard for accurate frequency determination. Spectra shown in the figures were normalized to specific peaks (indicated in the figure captions) and fluorescent backgrounds (usually not that intense) were subtracted using the baseline function in OriginPro8.

Conductivity Measurements. Conductivities were measured with a locally designed conductivity cell that consisted of two 0.64 mm diameter Pt wires fused within a 6 mm outer diameter, 4 mm inner diameter, and a flint glass rod and maintained at a constant distance. The cell constant was found to be 2.9 ± 0.2 cm^{-1}, as determined from a series of 0.01 and 0.1 M KCl$_{(aq)}$ standards at varying temperatures.

Electrochemistry. Electrochemical experiments were conducted using CH Instruments 618 or 760 potentiostats. Cyclic voltammograms were acquired on custom-made 3 mm Pt disk working electrodes, shrouded in Teflon sheaths, that were polished with 50 μm Al$_2$O$_3$, sonicated for 5 min in 18 MΩ purified water to remove Al$_2$O$_3$ particles, immersed in a 3:1 H$_2$SO$_4$:H$_2$O$_2$ Pirranha solution for 1 min to remove any remaining organics, rinsed with 18 MΩ purified water, and finally sonicated for an additional 5 min in 18 MΩ purified water before being dried in a 120 °C oven for at least 30 min prior to use. Three electrode cells were used with Mg ribbon counter and reference electrodes, scraped with a razor blade prior to immersion in the electrolytes. Electrochemical cells consisted of 25 mL three-neck round-bottom flasks using 1−2 mL of electrolyte. Galvanostatic deposition was done on a gold foil substrate, also in a three electrode cell with Mg reference and counter electrodes.

X-ray Diffraction (XRD). X-ray diffractograms were collected with a PANalytical XPert Pro MRD high resolution X-ray diffractometer with a Cu K$_\alpha$ X-ray source using fixed divergence slits incidence option and an X'Celerator detector.

Scanning Electron Microscopy (SEM) and Energy-Dispersive X-ray Spectroscopy (EDS). Surface morphology of electrodeposited magnesium was studied using scanning electron microscopy (SEM-XL 30 Environmental FEG) operating at 20 kV. Elemental analysis and elemental mapping were performed by using the EDX mode.

■ RESULTS AND DISCUSSION

Speciation of Mg^{2+} in IL Electrolytes As Determined by Raman Spectroscopy. Raman spectroscopy was used to study the speciation of Mg^{2+} in the various liquids examined, as well as to understand the solution environments of the other species present, including the TFSI$^-$ anions, the polyether chains, and the BH$_4^-$ anions. Figure S1 shows the Raman spectrum of an IL of composition [Mg-(BH$_4$)$_2$]$_{0.3}$[MPEG$_7$PyrTFSI]$_{0.7}$ over the entire spectral range examined. It provides a good overall representation for the spectra observed for the systems explored in this work. Four main regions of interest are highlighted in the figure and are discussed below and in the Supporting Information.

2000−2700 cm^{-1} B−H Stretching. The 2000−2700 cm^{-1} region contains B−H stretching modes that can be used to determine the state of coordination of BH$_4^-$ to Mg^{2+}.[34] Figure 1a shows the spectrum of this region for an IL containing
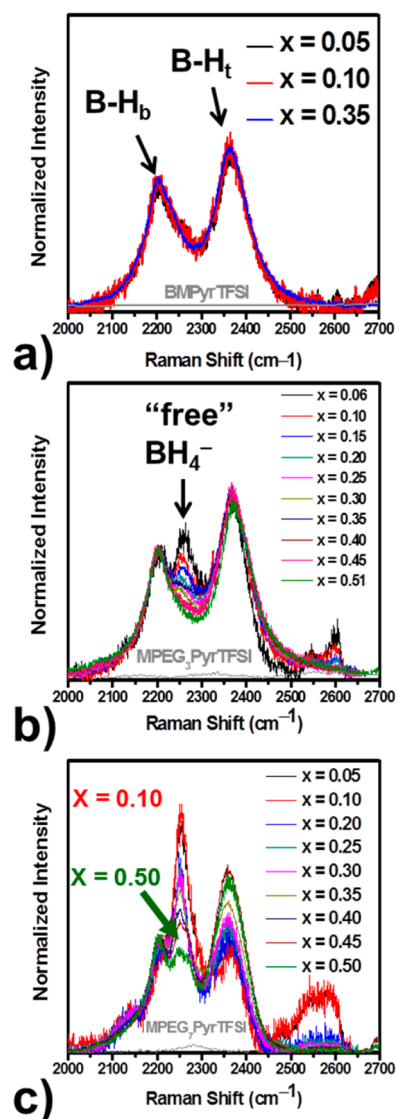

Figure 1. Raman spectra in the B−H stretching region at given molar fractions of Mg(BH$_4$)$_2$ (x) for (a) BMPyrTFSI, (b) MPEG$_3$PyrTFSI, and (c) MPEG$_7$PyrTFSI. Gray curves, without any peaks, in each figure are the spectra of the respective pure IL. All spectra were normalized using the 2200 cm^{-1} peak.

Mg(BH$_4$)$_2$ dissolved at various mole fractions in BMPyrTFSI. Raman bands are observed at 2200 and 2363 cm^{-1}. These are similar to those observed in many metal borohydride solutions and arise from BH$_4^-$ coordinated to metal ions. The lower frequency peak has been assigned to bridging B−H$_b$ vibrations while the higher frequency peak has been assigned to terminal B−H$_t$ vibrations.[14,34−37] The spectrum in Figure 1a shows that all BH$_4^-$ anions are coordinated in a bidentate fashion to the Mg^{2+} cation. These same spectral features are observed over a range of mole fractions of Mg(BH$_4$)$_2$ from 0.05 to 0.35, showing that BH$_4^-$ coordination at Mg^{2+} does not change over that range.

Figure 1b shows the same spectral region for $Mg(BH_4)_2$ in $MPEG_3PyrTFSI$ over a range of mole fractions. In addition to the bands for the bridging and terminal B−H vibrations, a new Raman band is observed at 2254 cm^{-1}. This band is more intense (relative to the B−H$_b$ and B−H$_t$ bands) at low mole fractions of $Mg(BH_4)_2$. Figure 1c shows that a similar band is observed for $Mg(BH_4)_2$ in $MPEG_7PyrTFSI$ over the entire mole fraction range explored. Again, the band intensity is higher relative to the B−H$_b$ and B−H$_t$ bands at lower mole fractions of $Mg(BH_4)_2$, and is more prominent than is observed in the $MPEG_3PyrTFSI$ system at equivalent compositions. We believe this band is due to "free" BH$_4^-$ (i.e., not coordinated to Mg^{2+}). To explore this assignment various materials containing BH$_4^-$ were examined in environments where one might expect "free" (i.e., unbound) BH$_4^-$.

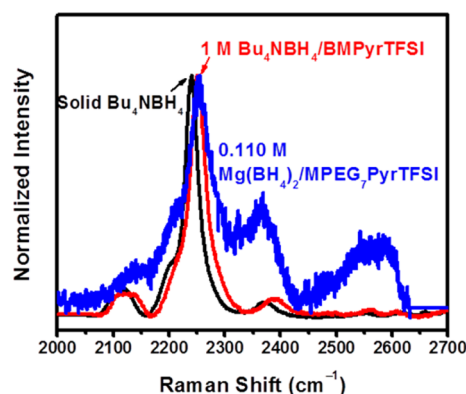Figure 2 shows the Raman spectrum of solid tetrabutylammonium borohydride (Bu_4NBH_4), 1 M Bu_4NBH_4 dissolved in

liquid ammonia.[35,38] A peak equivalent to the 2254 cm^{-1} peak is also observed in solid alkylammonium salts of the tetrahydroborate family.[39] For example, solid tetramethylammonium tetrahydroborate (Me_4NBH_4) shows a peak at 2268 cm^{-1}. Based on these previous observations, we assign the 2254 cm^{-1} band in Figures 1 and 2 to uncoordinated BH$_4^-$. These results show that some BH$_4^-$ is displaced from the Mg^{2+} center in these PEGylated ILs, with the extent of displacement increasing with the length of the polyether chain. This is consistent with conclusions from previous studies of $Mg(BH_4)_2$ in glyme solvents, and in a poly(ethylene oxide) (PEO) polymer matrix, which also suggested that some BH$_4^-$ dissociation was being caused by complexation from ether oxygens.[14,17] As described below, we believe this displacement of BH$_4^-$ impacts the electrochemical deposition/dissolution of the Mg^{2+}/Mg redox couple, generally improving the electrochemical behavior.

Comparison of the $MPEG_3PyrTFSI$ results (Figure 1b) with the $MPEG_7PyrTFSI$ results (Figure 1c) shows that the longer PEG chains in the latter are more effective at inducing displacement of the BH$_4^-$, as judged by the much more intense band for free BH$_4^-$ in $MPEG_7PyrTFSI$. This will be revisited below in comparing the electrochemical deposition/dissolution of Mg in these two ionic liquids.

780−920 cm^{-1} C−O−C Stretching and Mg−O Coordination. This spectral region shows bands associated with CH_2 rocking and C−O−C stretching modes for the PEG-IL systems.[40] Figure 3 shows this region as a function of $Mg(BH_4)_2$ mole fraction (x) in $[Mg(BH_4)_2]_x[MPEG_mPyrTFSI]_{1-x}$ solutions. The Raman band for the pure BMPyrTFSI IL is also shown. The dominant bands in this region in the PEGylated IL are those that make up the broad spectral feature that stretches from 780 to 860 cm^{-1}. These vibrational modes are attributed to the non-coordinating PEG chains, specifically to C−O−C stretches.[40] These were discussed previously by us in a study of polyether interactions with Mg^{2+}, where it was demonstrated that these modes shift when the polyether oxygens are coordinated to Mg^{2+}.[26] There is also a weak, broad feature from 780 to 850 cm^{-1} and a stronger, sharper feature centered at ca. 902 cm^{-1}, both attributed to the parent Pyr^+ cation moiety (both are observed in the BMPyrTFSI IL). Figure 3a shows the variation within this region as the mole fraction of $Mg(BH_4)_2$ is increased in the

Figure 2. Raman spectra in the B−H stretching region for solid Bu_4NBH_4 (black), 1 M Bu_4NBH_4/BMPyrTFSI (red), and 0.110 M $Mg(BH_4)_2$/$MPEG_7PyrTFSI$ (blue). All spectra in this figure were normalized to their most intense peak.

BMPyrTFSI and 0.110 M $Mg(BH_4)_2$ dissolved in $MPEG_7PyrTFSI$. Solid Bu_4NBH_4 shows a peak at 2250 cm^{-1}; 1 M Bu_4NBH_4 in BMPyrTFSI gives a peak at 2254 cm^{-1}, as does 0.110 M ($x = 0.05$) $Mg(BH_4)_2$ in $MPEG_7PyrTFSI$. These bands are consistent with those observed in previous Raman spectra for "free" (uncoordinated) BH$_4^-$. For example, $LiBH_4$ shows a peak at 2247 cm^{-1} in diethyl ether and 2265 cm^{-1} in
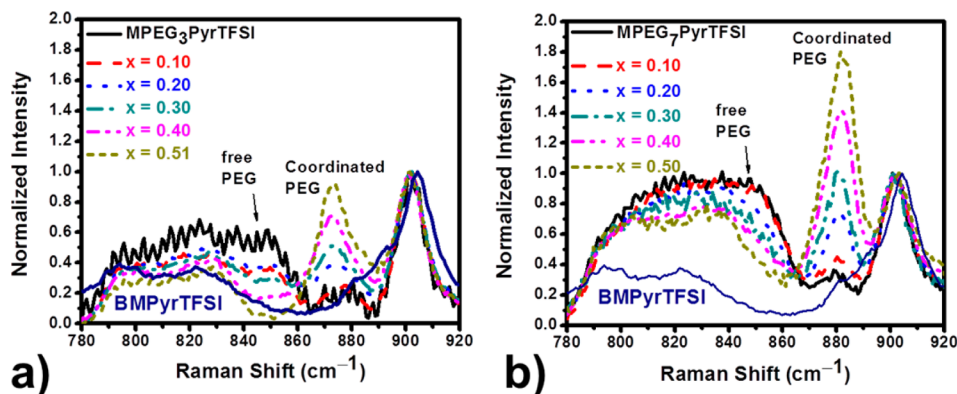

Figure 3. C−O−C stretching and CH_2 rocking regions for the two PEG-IL systems reported in this work. Each shows how the free and coordinated PEG modes change as the mole fraction of $Mg(BH_4)_2$ (x) is varied. (a) $[Mg(BH_4)_2]_x[MPEG_3PyrTFSI]_{1-x}$ and (b) $[Mg(BH_4)_2]_x[MPEG_7PyrTFSI]_{1-x}$. The spectra in this region for BMPyrTFSI is shown in navy blue and labeled in each figure. Each spectrum was normalized to its respective ca. 902 cm^{-1} (Pyr^+) peaks.

MPEG$_3$PyrTFSI system. At more dilute concentrations of Mg(BH$_4$)$_2$, and in the pure PEG-IL, the dominant bands are those that make up the broad feature from 780 to 860 cm^{-1}. These vibrational modes are attributed to the non-coordinating (free) PEG chains. The peak arising at ca. 875 cm^{-1} is produced when the PEG chains are coordinated to Mg^{2+}. Mg^{2+} coordination also causes the broad feature due to vibrations from unbound polyether C—O—C groups to decrease, as can be seen in the figure. This coordination behavior between Mg^{2+} (from Mg(BH$_4$)$_2$) and the ether oxygen chains is reminiscent of the observations made for Mg(TFSI)$_2$/BMPyrTFSI, to which glyme chelators were added.[26] In Figure 3b the same region is shown for the MPEG$_7$PyrTFSI system. Again, it is evident that free PEG modes are reduced, and the coordinated PEG mode(s) enhanced, as the Mg(BH$_4$)$_2$ mole fraction is increased. However, the increase in the coordinated peak (ca. 880 cm^{-1}) in the MPEG$_7$PyrTFSI system is more dramatic, while the decrease in the free PEG band is more subtle, as the fraction of Mg(BH$_4$)$_2$ is increased. This suggests that the fraction of ether oxygens involved in coordinating Mg^{2+} is higher in the MPEG$_7$PyrTFSI system, meaning that this fraction depends on the chain length and coordination from other ligands. The present results show that the PEG chains do in fact chelate the Mg^{2+} species, despite the close proximity of the positive charge from the parent pyrrolidinium moiety.

715−775 cm^{-1} Coordination-Sensitive TFSI$^-$. We previously described a Raman study of the coordination of TFSI$^-$ at Mg^{2+} in various ionic liquids.[26] That analysis depends on quantification of several Raman bands in the 715−775 cm^{-1} region. Specifically, a band at 742 cm^{-1} is attributed to free (non-metal ion coordinating) TFSI$^-$, and a band at 752 cm^{-1} is attributed to Mg^{2+} coordinated TFSI$^-$.[26,41−49] Analysis of the relative intensities of these bands (and others in this region) provides information about the number of TFSI$^-$ species coordinated per Mg^{2+} (and the state of the coordinated TFSI$^-$ such as mono- versus bidentate coordination and coordination in aggregate ion pairs).[26,41−49] We refer to the number of coordinated TFSI$^-$ anions per Mg^{2+} center as the solvation number, n. Figure 4a shows how the 752 cm^{-1} band attributed to TFSI$^-$ coordinated to Mg^{2+} increases as the Mg(BH$_4$)$_2$ mole fraction is increased in the BMPyrTFSI IL. This shows that TFSI$^-$ coordinates to Mg^{2+} under these conditions. Figure 4b shows a plot derived from these data giving the fraction of coordinated TFSI$^-$ versus mole fraction of Mg(BH$_4$)$_2$. The fraction of TFSI$^-$ coordinated to Mg^{2+} was found by integrating under the areas of Voigt peak fits for the raw data. An example fit is shown in Figure S3. These fits are consistent with previous work on Mg-TFSI systems.[25,26,31] Also plotted in Figure 4b are theoretical curves that correspond to what would be expected for one, two or three coordinated TFSI$^-$ species per Mg^{2+} at given mole fractions of a MgX$_2$ salt (X ≠ TFSI$^-$), obtained using a previously published treatment.[26] The data for Mg(BH$_4$)$_2$ agree with the n = 1 curve, showing that one TFSI$^-$ coordinates to Mg^{2+} for the full composition range (note: the x = 0.40 composition resulted in a solid at room temperature, all other mixtures were liquids). These data show that under these conditions both TFSI$^-$ and BH$_4^-$ are coordinated to Mg(II).

Figure 4b also shows data derived from experiments using Mg(ClO$_4$)$_2$ as the Mg^{2+} source. These data show that the solvation number for TFSI$^-$ is two in this case, suggesting that ClO$_4^-$ is more weakly bound than BH$_4^-$, which appears to lead to displacement of one of the two ClO$_4^-$ anions under these
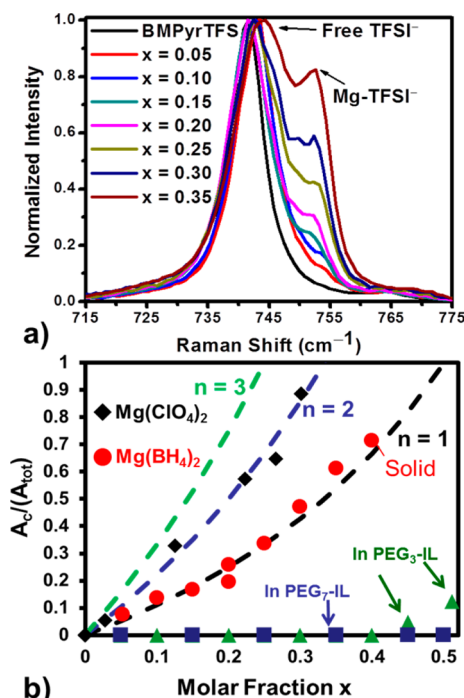

Figure 4. (a) Raman spectra (715−775 cm^{-1}) for [Mg-(BH$_4$)$_2$]$_x$[BMPyrTFSI]$_{1-x}$ electrolytes. (b) Fraction of TFSI$^-$ in coordination with Mg^{2+} (A_c/A_{tot}) as a function of the molar fraction (x) of Mg(BH$_4$)$_2$ (red circles) and Mg(ClO$_4$)$_2$ (black diamonds) in BMPyrTFSI. Also shown are values for a series of Mg(BH$_4$)$_2$/MPEG$_3$PyrTFSI electrolytes (green triangles) and Mg(BH$_4$)$_2$/MPEG$_7$PyrTFSI electrolytes (blue squares). Dashed lines represent the theoretical trends for the average number of TFSI$^-$ coordinating Mg^{2+} (n) for n = 1, 2, and 3.

conditions. This shows that this speciation analysis allows differentiation of systems that behave differently with respect to anion binding to the metal center.

Figure 4b also shows data for a range of compositions from the [Mg(BH$_4$)$_2$]$_x$[MPEG$_3$PyrTFSI]$_{1-x}$ and [Mg-(BH$_4$)$_2$]$_x$[MPEG$_7$PyrTFSI]$_{1-x}$ systems. These data show that there is no detectable TFSI$^-$ coordination to Mg^{2+} up to x = 0.4 in the MPEG$_3$PyrTFSI system, and very little above that value (up to a 1:1 mixture of Mg(BH$_4$)$_2$ with the MPEG$_3$PyrTFSI IL). For the MPEG$_7$PyrTFSI, there is no detectable TFSI$^-$ coordination up to x = 0.5. This suggests that the PEGylated ILs are very effective at sequestering Mg^{2+} and preventing its coordination by TFSI$^-$.

Figure 5 shows spectra in this same region for a number of different solutions of Mg(BH$_4$)$_2$ at various (high concentration) mole fractions in BMPyrTFSI, MPEG$_3$PyrTFSI, and MPEG$_7$PyrTFSI. No evidence for coordinated TFSI$^-$ (or a small degree of coordination at high concentrations of Mg(BH$_4$)$_2$ in MPEG$_3$PyrTFSI) is observed except in BMPyrTFSI, showing that quite high concentrations of Mg^{2+} species can be obtained in the PEG-IL media without inducing TFSI$^-$ coordination. As described below, we believe the suppression of TFSI$^-$ coordination at Mg^{2+} in these PEGylated ILs provides some protection against TFSI$^-$ fragmentation under reducing conditions, which improves the electrochemical performance of Mg cycling.

Electrochemical Performance of Mg^{2+}/Mg in ILs. Figure 6 shows repetitive cyclic voltammograms for Mg deposition/dissolution for a solution of Mg(BH$_4$)$_2$ in
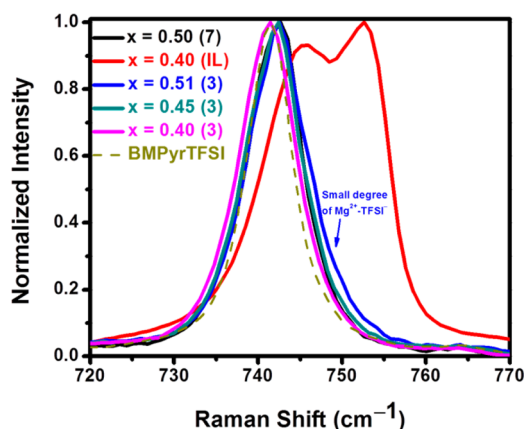
Figure 5. 715−775 cm^{-1} region comparing electrolytes with given mole fractions of Mg(BH$_4$)$_2$ (indicated by x) in the different IL systems (notated in the figure as (7) for MPEG$_7$PyrTFSI, (IL) for BMPyrTFSI, and (3) for MPEG$_3$PyrTFSI). The 742 cm^{-1} mode is also shown for pure BMPyrTFSI (gold dashed curve).

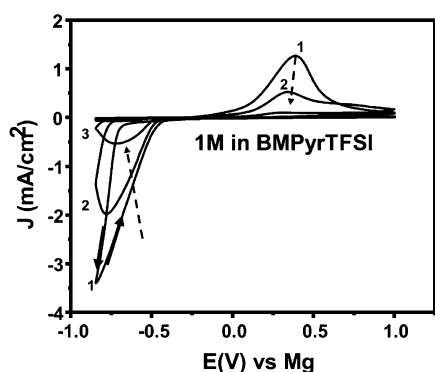**Figure 6.** Successive cyclic voltammograms for 1 M Mg(BH$_4$)$_2$/BMPyrTFSI, at 25 mV/s.

BMPyrTFSI. As can be seen, the deposition is not reversible, with rapid suppression of the electrochemical response from Mg. This behavior is typical for Mg in systems containing TFSI$^-$.[24] Figure 7 shows the cyclic voltammograms for electrochemical deposition/dissolution of Mg from Mg(BH$_4$)$_2$ in solutions of either the MPEG$_3$TFSI IL or the MPEG$_7$TFSI IL. Many different mole fractions of Mg(BH$_4$)$_2$ in these ILs
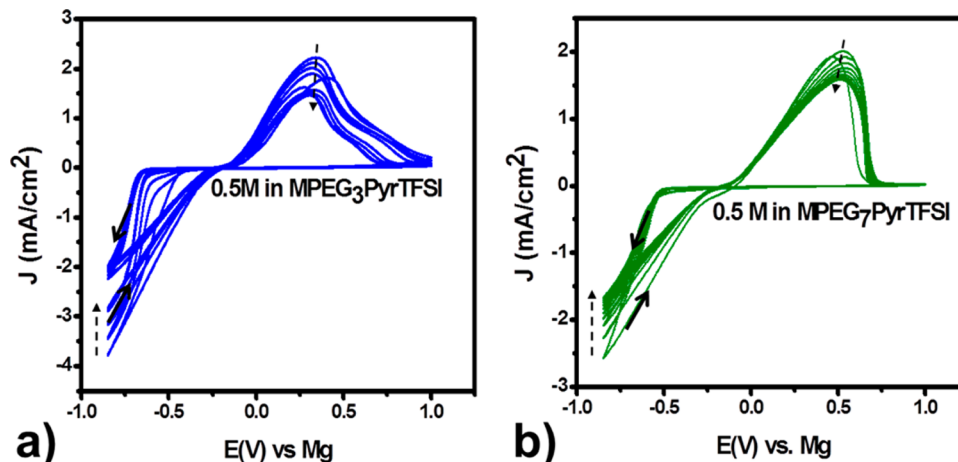
were examined. The data for other concentrations are given in Figures S4−S6. The concentrations shown in Figures 6 and 7 were the ones that gave the highest current densities. The room temperature conductivities for these solutions were 0.5 ± 0.1 mS/cm^2, 0.38 ± 0.01 mS/cm^2, and 0.24 ± 0.02 mS/cm^2 for the 1 M Mg(BH$_4$)$_2$/BMPyrTFSI, 0.5 M Mg(BH$_4$)$_2$/MPEG$_3$PyrTFSI, and 0.5 M Mg(BH$_4$)$_2$/MPEG$_7$PyrTFSI, respectively. These conductivities are an order of magnitude lower than typical Li-ion electrolytes but still relatively high considering the high viscosities of the media. The relationship between current density and mole fraction of Mg(BH$_4$)$_2$ is complicated for these IL solutions, since increasing Mg(BH$_4$)$_2$ leads to viscosity increases that can reduce the current density. Figure 8 shows plots of Coulombic efficiency and stripping
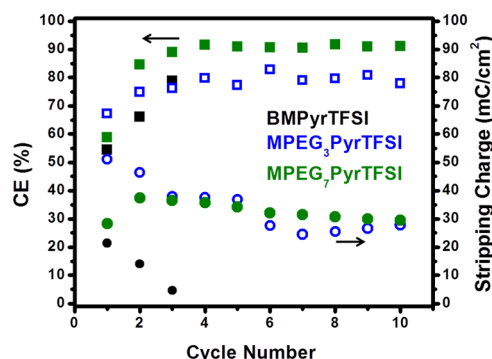

Figure 8. Coulombic efficiencies (CE) (squares) and stripping charges (circles) for each cycle in the given systems (from Figures 6 and 7). Data for the BMPyrTFSI electrolyte are presented as solid black data points. Data for the MPEG$_3$PyrTFSI are presented as open blue data points. Data for the MPEG$_7$PyrTFSI electrolyte are presented as solid green data points.

charge versus cycle number for the experiments shown in Figures 6 and 7. These results show a marked improvement in reversibility of the deposition process compared to the data in Figure 6.

Oxidative stability of the electrolyte is also important to the electrochemical performance of a battery electrolyte. Oxidative stability can affect the choice of cathode material and current collector. We measured the oxidative stability for the 0.5 M Mg(BH$_4$)$_2$/MPEG$_7$PyrTFSI electrolyte (the electrolyte with

Figure 7. Successive cyclic voltammograms for (a) 0.5 M Mg(BH$_4$)$_2$/MPEG$_3$PyrTFSI and (b) 0.5 M Mg(BH$_4$)$_2$/MPEG$_7$PyrTFSI, at 25 mV/s.

the best electrochemical characteristics), using linear sweep voltammetry (LSV). Results show that the potential of oxidation varies with the chosen electrode (Figure S7). We found the Mg(BH$_4$)$_2$/MPEG$_7$PyrTFSI electrolyte to be most stable on stainless steel 316 followed by glassy carbon. It was least stable on the two noble metal electrodes used (Pt and Au). This oxidative stability trend is actually the opposite of that found for Grignard-based Mg battery electrolytes, as they tend to corrode steel.[9] These oxidative stability findings correlate well with previous findings for Mg(BH$_4$)$_2$ in ethereal solvents.[14]

The conditions in Figure 7b were used for a galvanostatic deposition of Mg at 0.1 mA/cm^2 for 16 h, followed by characterization of the deposit. The first 15 min of the potential versus time trace for this experiment is shown in Figure S8. Figure 9 shows the XRD for the deposit. The XRD pattern
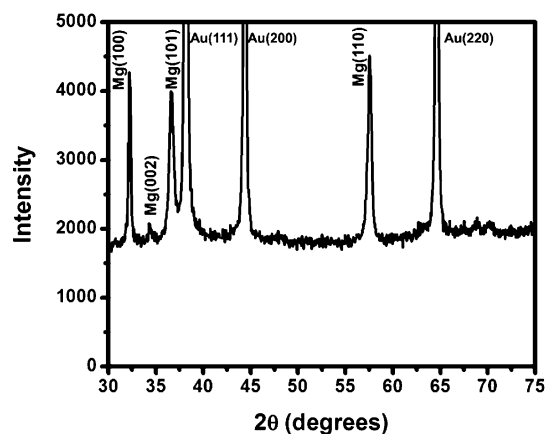
Figure 9. XRD pattern showing Mg deposit and Au substrate peaks.

reveals a preferred orientation of the deposited Mg which is consistent with previous literature findings.[50] The Mg(002) diffraction peak is much weaker than the Mg(100), Mg(101), and Mg(110) peaks. The Au K$_\alpha$ peaks from the substrate are far more intense than the Mg peaks and are cut off before their respective peak intensities. The XRD demonstrates deposition of metallic Mg, with no evidence for other phases being present.

Figure 10a−c shows successively closer views of the deposit obtained by SEM. Figure 10c gives a good representation of the Mg surface morphology which appears to be relatively smooth, without sign of dendritic growths. Figure 10d gives the EDS
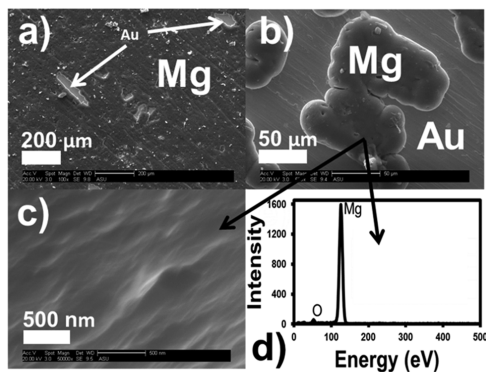
Figure 10. SEM images at (a) 100×, (b) 500×, and (c) 50000×, and (d) EDS spectrum for sample portion in image (e).

spectrum from an area in which no underlying Au substrate is exposed. A very strong Mg peak is observed along with a very weak O peak from the native oxide on the Mg surface, consistent with Mg deposition and absence of oxide precipitation or competing reduction processes such as TFSI$^-$ reduction, which leads to surface fouling (see below). The data show no evidence of trace carbon in the Mg deposit which suggests the polyether chains are stable against reduction in these systems. In the Supporting Information, EDS elemental maps are shown for the area in Figure 10b which reinforce the lack of significant oxygen associated with the deposit (Figure S9). The analogous deposition experiment with 0.75 M Mg(BH$_4$)$_2$ in BMPyrTFSI gave a deposit with significant C, F, S, and O content as determined by EDS. The EDS spectrum of this deposit is shown in Figure S10. These results suggest that deposition in the Mg(BH$_4$)$_2$/BMPyrTFSI solution produces substantial decomposition of TFSI$^-$ and consequent surface fouling while the 0.5 M Mg(BH$_4$)$_2$/MPEG$_7$PyrTFSI deposition condition produces a "clean" Mg deposit with no evidence of TFSI$^-$ fragmentation or surface fouling.

Effects of Mg^{2+} Speciation on Electrochemical Behavior. The data above represent the first demonstration of reversible electrochemical deposition/dissolution of bulk Mg in a task-specific ionic liquid system. They show that high Coulombic efficiencies (≥90%) can be obtained under these conditions, and that deposition can be achieved without significant surface fouling. These results are now discussed within the context of past experimental and theoretical studies of Mg^{2+} speciation and resulting reactivity in a variety of systems.

Taken together, the spectroscopic data shown here, and the previous Raman study[26] of Mg(TFSI)$_2$ dissolved in BMPyrTF-SI or glyme-containing BMPyrTFSI, reveal that Mg^{2+} speciation in IL systems is both measurable and controllable. For ILs containing only TFSI$^-$ anions and no ether or polyether solvents, Mg^{2+} is typically found as Mg(TFSI)$_3^-$. If polyether solvents or ionic liquid cations bearing pendent polyether chains are added such that the molar ratio of the total number of ether oxygens to Mg^{2+} is large (e.g., >5 or 6), the ether oxygens displace TFSI$^-$, producing free TFSI$^-$ and Mg^{2+} bound in a neutral coordination environment of ether oxygens. The number of ether oxygens needed to fully displace all TFSI$^-$ anions depends on the length of the polyether chain and its relative concentration. The ease with which ether oxygens displace TFSI$^-$ is due to the relatively weak binding of TFSI$^-$ to Mg^{2+}.[16] For polyether solvents, TFSI$^-$ displacement has been shown to improve the electrochemical behavior of the Mg^{2+}/Mg redox system.[51−53]

The situation when the source of Mg^{2+} is Mg(BH$_4$)$_2$ rather than Mg(TFSI)$_2$ is similar, though there are important differences. As shown above, when Mg(BH$_4$)$_2$ is dissolved in ILs containing TFSI$^-$, some TFSI$^-$ coordination will occur. If polyether chains pendent on IL cations are present, TFSI$^-$ will be displaced. If the ratio of ether oxygens to Mg^{2+} is sufficiently high, there is also significant displacement of BH$_4^-$ from the Mg^{2+} center. Without Raman scattering cross sections for the bound and free BH$_4^-$ species, one cannot quantitatively obtain the degree of dissociation of BH$_4^-$ in these conditions. However, the data in Figure 1c suggest that substantial displacement of at least one of the bound BH$_4^-$ anions occurs when a sufficient number of polyether oxygens are present. In this case one possible speciation for Mg^{2+} would be [(PEG)Mg(BH$_4$)]$^+$, where PEG represents a generic polyether

Table 1. Comparison of Data for Mg Deposition/Dissolution in $Mg(BH_4)_2$ Electrolytes[a]

| medium | C (M) | CE (%) | | Cyc 1 | | |
		Cyc 1	Cyc 10	J_a (mA/C·m^2)	ν (mV/s)	ref
G4	0.01	84	NA	0.3	20	17
G3	0.01	81	NA	0.075	20	17
G2	0.01	77	NA	0.05	20	17
G1 (DME)	0.1	67	NA	0.25	5	14
THF	0.5	40	NA	0.032	5	14
0.6 M LiBH$_4$/G1	0.18	94	NA	25	5	14
1.5 M LiBH$_4$/G2	0.1	99	NA	12.5	20	11
PEO @ 100 °C	10 wt %	98	NA	0.3	20	17
BMPyrTFSI	1	55	NA	1.25	25	present work
MPEG$_3$PyrTFSI	0.5	67	78	2	25	Present work
MPEG$_7$PyrTFSI	0.5	59	90	2	25	Present work

[a]C is the concentration of $Mg(BH_4)_2$, Cyc 1 and Cyc 10 denote the first and tenth consecutive cycles for acquired CVs, respectively, CE is coulombic efficiency in the respective cycles, J_a is the anodic current density for the stripping current, and ν is the scan rate used.

chain or chains. This type of speciation was suggested in an earlier study of $Mg(BH_4)_2$ in a PEO matrix.[17] In that case, reversible electrochemical deposition and dissolution of Mg was observed with good Coulombic efficiency. We also examined the Raman spectra and electrochemistry for solutions of $[Mg(TFSI)_2]_x[MPEG_7PyrTFSI]_{1-x}$ over a range of x values. For the range of x values from 0 to 0.5, the Raman data show no evidence for TFSI$^-$ coordination, implying efficient displacement of TFSI$^-$ by the polyether chains when a sufficient supply of polyether oxygens are present. This is shown in Figure S11. However, the electrochemical deposition and dissolution of Mg in this medium is not reversible (Figure S12). These results suggest that the PEGylated ILs provide a coordination environment conducive to reversible Mg^{2+}/Mg electrochemistry, so long as BH$_4^-$ is present.

Table 1 compares results from a variety of past studies with those presented here. With the exception of systems containing LiBH$_4$ additive, only one previous study shows a higher CE, which is for the case of $Mg(BH_4)_2$ incorporated into a PEO matrix.[17] However, even at a temperature of 100 °C, that system only provides a current density of 0.3 mA/cm^2, nearly an order of magnitude lower than that reported here. The best current densities for previous studies of $Mg(BH_4)_2$ in ether solvents are also an order of magnitude lower than those reported here. We believe the high currents observed in the present work result from the high concentration of $Mg(BH_4)_2$ that can be dissolved in these PEGylated ILs. Two entries in the table report high CE and current density values for cases with added LiBH$_4$. Those are not discussed further since the presence of Li$^+$ can lead to a variety of effects not related to Mg^{2+} speciation.[18]

We believe the attractive electrochemical performance observed in the present case is related to Mg^{2+} speciation in the PEGylated ILs. There may be a variety of ways in which speciation influences CE. We speculate on a few here. The first is through displacement of TFSI$^-$ from the Mg^{2+} center to prevent unwanted reactions of TFSI$^-$. There have been previous discussions of the potentially beneficial effects of removal of TFSI$^-$ from the primary coordination sphere of Mg^{2+}. This was discussed by Rajput et al., who presented theoretical results suggesting that TFSI$^-$ coordination to Mg^{2+} during the electrodeposition process might lead to transient formation of a Mg(I)-TFSI$^-$ radical intermediate that could lead to reductive fragmentation of the TFSI$^-$ anion.[16] Their quantum chemical calculations predicted that fragmentation of

TFSI$^-$ in this intermediate was exothermic, suggesting a likely decomposition pathway. This might lead to Coulombic inefficiencies and surface fouling due to accumulation of the resulting fragments at the interface. The present results are entirely consistent with those findings. We observe the highest CE for the $Mg(BH_4)_2$/MPEG$_7$PyrTFSI system in which TFSI$^-$ displacement from the Mg^{2+} center was essentially complete. EDS examination of the Mg deposit shows no detectable TFSI$^-$ fragmentation products (Figure 10). In contrast, we observe irreversible cycling and high atomic populations of C, O, F, and S for deposits formed in cases where TFSI$^-$ is coordinated to the Mg^{2+} center (Figure S10).

A second effect relevant to achievement of high Coulombic efficiencies for Mg electrodeposition/dissolution may relate to the elimination of trace water in the electrolyte. Many of the electrolyte systems that have been reported to support reversible Mg deposition/dissolution are ones with intrinsic chemical reactivity toward water. Such reactivity should scavenge water from the electrolyte, preventing its delivery to the Mg interface and production of a passivating MgO layer. For example, two of the electrolyte systems that have shown good reversibility for Mg include Grignard systems and $Mg(BH_4)_2$, both of which are reactive toward water. We speculate that the achievement here of good Coulombic efficiency and lack of surface blocking is likely aided by the consumption of trace water in the electrolyte by BH$_4^-$. It also seems likely that the MPEG$_7$PyrTFSI ionic liquid has the best performance due to its higher concentration of free BH$_4^-$, which is likely to be more reactive toward water than BH$_4^-$ bound to Mg^{2+}.

The third way in which the PEGylated ILs may improve Mg electrochemical performance is through the production of cationic speciation for Mg^{2+} and the favorable impact of this on transport. As discussed above, the Raman data for $Mg(BH_4)_2$/MPEG$_7$PyrTFSI electrolytes are consistent with speciation of Mg^{2+} as $(PEG)Mg(BH_4)^+$. This cationic state will facilitate electromigration toward the Mg electrode under deposition conditions and away from it under dissolution conditions, which should favor high currents.

■ CONCLUSIONS

We have synthesized task specific ILs that bear pendent polyether chains designed to complex Mg^{2+} from a $Mg(BH_4)_2$ source. This complexation changes the speciation of Mg^{2+} in these media, which was characterized using Raman spectros-

copy. Specifically, polyether complexation prevents TFSI⁻ coordination at Mg^{2+} and also generates free BH_4^- for the $Mg(BH_4)_2/MPEG_7PyrTFSI$ IL. These speciation changes produce superior electrochemical behavior compared to that in BMPyrTFSI or previously reported electrolyte systems containing ether or polyether solvents. These PEGylated IL electrolytes give Mg deposition/dissolution with high CE and very high current density. The Mg deposits are characterized by high purity (i.e., no detectable surface fouling) and lack of dendritic growth. These results represent the first demonstration of reversible electrochemical deposition/dissolution of Mg in an ionic liquid designed specifically for improved electrochemical performance.

We speculate on three specific possible origins of the improved electrochemical performance of these systems that derive from the observed speciation changes. These include suppression of reductive decomposition pathways for TFSI⁻ that may cause low CE and/or surface fouling, decrease of trace water concentrations in the electrolyte that may react with Mg and produce passivating films of MgO, and the generation of cationic speciation for Mg^{2+} that enhances transport by electromigration. All of these possible mechanisms provide guidance for future efforts to improve Mg battery chemistries.

■ ASSOCIATED CONTENT

Ⓢ Supporting Information

The Supporting Information is available free of charge on the ACS Publications website at DOI: 10.1021/jacs.5b11031.

> Further representative Raman data, CVs and LSVs of $Mg(BH_4)_2$ systems, galvanostatic deposition results, and NMR of the synthesized ionic liquids, including Figures S1−S12 (PDF)

■ AUTHOR INFORMATION

Corresponding Author

*dan.buttry@asu.edu

Notes

The authors declare no competing financial interest.

■ ACKNOWLEDGMENTS

■ REFERENCES

(1) Yoo, H. D.; Shterenberg, I.; Gofer, Y.; Gershinsky, G.; Pour, N.; Aurbach, D. *Energy Environ. Sci.* **2013**, *6*, 2265.

(2) Mohtadi, R.; Mizuno, F. *Beilstein J. Nanotechnol.* **2014**, *5*, 1291.

(3) Muldoon, J.; Bucur, C. B.; Gregory, T. *Chem. Rev.* **2014**, *114*, 11683.

(4) Park, M.-S.; Kim, J.-G.; Kim, Y.-J.; Choi, N.-S.; Kim, J.-S. *Isr. J. Chem.* **2015**, *55*, 570.

(5) Liu, T.; Cox, J. T.; Hu, D.; Deng, X.; Hu, J.; Hu, M. Y.; Xiao, J.; Shao, Y.; Tang, K.; Liu, J. *Chem. Commun. (Cambridge, U. K.)* **2015**, *51*, 2312.

(6) Muldoon, J.; Bucur, C. B.; Oliver, A. G.; Sugimoto, T.; Matsui, M.; Kim, H. S.; Allred, G. D.; Zajicek, J.; Kotani, Y. *Energy Environ. Sci.* **2012**, *5*, 5941.

(7) Muldoon, J.; Bucur, C. B.; Oliver, A. G.; Zajicek, J.; Allred, G. D.; Boggess, W. C. *Energy Environ. Sci.* **2013**, *6*, 482.

(8) Lv, D.; Xu, T.; Saha, P.; Datta, M. K.; Gordin, M. L.; Manivannan, a.; Kumta, P. N.; Wang, D. *J. Electrochem. Soc.* **2013**, *160*, A351.

(9) Yagi, S.; Tanaka, a.; Ichikawa, Y.; Ichitsubo, T.; Matsubara, E. *J. Electrochem. Soc.* **2013**, *160*, C83.

(10) Aurbach, D.; Gizbar, H.; Schechter, A.; Chusid, O.; Gottlieb, H. E.; Gofer, Y.; Goldberg, I. *J. Electrochem. Soc.* **2002**, *149*, A115.

(11) Shao, Y.; Liu, T.; Li, G.; Gu, M.; Nie, Z.; Engelhard, M.; Xiao, J.; Lv, D.; Wang, C.; Zhang, J.-G.; Liu, J. *Sci. Rep.* **2013**, *3*, 3130.

(12) Tuerxun, F.; Abulizi, Y.; NuLi, Y.; Su, S.; Yang, J.; Wang, J. *J. Power Sources* **2015**, *276*, 255.

(13) Mohtadi, R. Borohydride Solvo-Ionic Liquid Family For Magnesium Battery. U.S. Patent US20150072250 A1, 2015

(14) Mohtadi, R.; Matsui, M.; Arthur, T. S.; Hwang, S.-J. *Angew. Chem., Int. Ed.* **2012**, *51*, 9780.

(15) Shterenberg, I.; Salama, M.; Gofer, Y.; Levi, E.; Aurbach, D. *MRS Bull.* **2014**, *39*, 453.

(16) Rajput, N. N.; Qu, X.; Sa, N.; Burrell, A. K.; Persson, K. A. *J. Am. Chem. Soc.* **2015**, *137*, 3411.

(17) Shao, Y.; Rajput, N. N.; Hu, J.; Hu, M.; Liu, T.; Wei, Z.; Gu, M.; Deng, X.; Xu, S.; Han, K. S.; Wang, J.; Nie, Z.; Li, G.; Zavadil, K. R.; Xiao, J.; Wang, C.; Henderson, W. a.; Zhang, J.-G.; Wang, Y.; Mueller, K. T.; Persson, K.; Liu, J. *Nano Energy* **2015**, *12*, 750.

(18) Chang, J.; Haasch, R. T.; Kim, J.; Spila, T.; Braun, P. V.; Gewirth, A. a; Nuzzo, R. G. *ACS Appl. Mater. Interfaces* **2015**, *7*, 2494.

(19) MacFarlane, D. R.; Tachikawa, N.; Forsyth, M.; Pringle, J. M.; Howlett, P. C.; Elliott, G. D.; Davis, J. H.; Watanabe, M.; Simon, P.; Angell, C. A. *Energy Environ. Sci.* **2014**, *7*, 232.

(20) NuLi, Y.; Yang, J.; Wang, J.; Xu, J.; Wang, P. *Electrochem. Solid-State Lett.* **2005**, *8*, C166.

(21) NuLi, Y.; Yang, J.; Wang, P. *Appl. Surf. Sci.* **2006**, *252*, 8086.

(22) Zhao, Q.; NuLi, Y.; Nasiman, T.; Yang, J.; Wang, J. *Int. J. Electrochem.* **2012**, *2012*, 1.

(23) Lodovico, L.; Martins, V. L.; Benedetti, T. M.; Torresi, R. M. *J. Braz. Chem. Soc.* **2014**, *25*, 460.

(24) Vardar, G.; Sleightholme, A. E. S.; Naruse, J.; Hiramatsu, H.; Siegel, D. J.; Monroe, C. W. *ACS Appl. Mater. Interfaces* **2014**, *6*, 18033.

(25) Giffin, G.; Moretti, A.; Jeong, S.; Passerini, S. *J. Phys. Chem. C* **2014**, *118*, 9966.

(26) Watkins, T.; Buttry, D. A. *J. Phys. Chem. B* **2015**, *119*, 7003.

(27) Venkata Narayanan, N. S.; Ashok Raj, B. V.; Sampath, S. *Electrochem. Commun.* **2009**, *11*, 2027.

(28) Narayanan, N. S. V.; Ashok Raj, B. V.; Sampath, S. *J. Power Sources* **2010**, *195*, 4356.

(29) Murase, K.; Sasaki, I.; Kitada, a.; Uchimoto, Y.; Ichii, T.; Sugimura, H. *J. Electrochem. Soc.* **2013**, *160*, D453.

(30) Kar, M.; Winther-Jensen, B.; Forsyth, M.; MacFarlane, D. R. *Phys. Chem. Chem. Phys.* **2013**, *15*, 7191.

(31) Giffin, G. a.; Tannert, J.; Jeong, S.; Uhl, W.; Passerini, S. *J. Phys. Chem. C* **2015**, *119*, 5878−5887.

(32) Dobbelin, M.; Azcune, I.; Luzuriaga, A. R.; Genua, A.; Jovanovski, V.; Odriozola, I.; et al. *Chem. Mater.* **2012**, *24*, 1583.

(33) Ganapatibhotla, L. V. N. R.; Zheng, J.; Roy, D.; Krishnan, S. *Chem. Mater.* **2010**, *22*, 6347.

(34) Marks, T. J.; Kolb, J. R.; Introduction, I. *Chem. Rev.* **1977**, *77*, 263.

(35) Shirk, a. E.; Shriver, D. F. *J. Am. Chem. Soc.* **1973**, *95*, 5901.

(36) Marks, T. J.; Kennelly, W. J.; Kolb, J. R.; Shimp, L. a. *Inorg. Chem.* **1972**, *11*, 2540.

(37) Davies, N.; Bird, P. H.; Wallbridge, M. G. H. *J. Chem. Soc. A* **1968**, 2269.

(38) Emery, A. R.; Taylor, R. C. *J. Chem. Phys.* **1958**, *28*, 1029.

(39) Dalton, D. A.; Somayazulu, M.; Goncharov, A. F.; Hemley, R. J. *J. Phys. Chem. A* **2011**, *115*, 11033.

(40) Brouillette, D.; Irish, D. E.; Taylor, N. J.; Perron, G.; Odziemkowski, M.; Desnoyers, J. E. *Phys. Chem. Chem. Phys.* **2002**, *4*, 6063.

(41) Monteiro, M. J.; Bazito, F. F. C.; Siqueira, L. J. a; Ribeiro, M. C. C.; Torresi, R. M. *J. Phys. Chem. B* **2008**, *112*, 2102.

(42) Lassègues, J.-C.; Grondin, J.; Talaga, D. *Phys. Chem. Chem. Phys.* **2006**, *8*, 5629.

(43) Lassègues, J.; Grondin, J.; Aupetit, C.; Johansson, P. *J. Phys. Chem. A* **2009**, *113*, 305.

(44) Duluard, S.; Grondin, J.; Bruneel, J.; Pianet, I.; Gréland, A.; Campet, G.; Lasségues, J.; et al. *J. Raman Spectrosc.* **2008**, *39*, 627.

(45) Umebayashi, Y.; Mitsugi, T.; Fukuda, S.; Fujimori, T.; Fujii, K.; Kanzaki, R.; Takeuchi, M.; Ishiguro, S.-I. *J. Phys. Chem. B* **2007**, *111*, 13028.

(46) Castriota, M.; Caruso, T.; Agostino, R. G.; Cazzanelli, E.; Henderson, W. A.; Passerini, S. *J. Phys. Chem. A* **2005**, *109*, 92.

(47) Hardwick, L. J.; Holzapfel, M.; Wokaun, A.; Novak, P. *J. Raman Spectrosc.* **2007**, *38*, 110.

(48) Borodin, O.; Smith, G. D.; Henderson, W. *J. Phys. Chem. B* **2006**, *110*, 16879.

(49) Herstedt, M.; Smirnov, M.; Johansson, P.; Chami, M.; Grondin, J.; Servant, L.; Lassègues, J. C. *J. Raman Spectrosc.* **2005**, *36*, 762.

(50) Tutusaus, O.; Mohtadi, R.; Arthur, T. S.; Mizuno, F.; Nelson, E. G.; Sevryugina, Y. V. *Angew. Chem., Int. Ed.* **2015**, *54*, 7900.

(51) Ha, S.; Lee, Y.; Woo, S. W.; Koo, B.; Kim, J.; Cho, J.; Lee, K. T.; Choi, N. *ACS Appl. Mater. Interfaces* **2014**, *6*, 4063.

(52) Kitada, A.; Kang, Y.; Uchimoto, Y.; Murase, K. *J. Electrochem. Soc.* **2014**, *161*, D102.

(53) Fukutsuka, T.; Asaka, K.; Inoo, A.; Yasui, R.; Miyazaki, K.; Abe, T.; Nishio, K.; Uchimoto, Y. *Chem. Lett.* **2014**, *43*, 1788.